Article

Locating the missing absorption enhancement due to multi–core black carbon aerosols

Xiyao Chen[1], Joseph Ching [2], Feng Wu [3], Hitoshi Matsui [4], Mark Z. Jacobson [5], Fan Zhang [1], Yuanyuan Wang[1], Zexuan Zhang[1], Dantong Liu[1], Shupeng Zhu [1], Yinon Rudich [6], Zongbo Shi [7], Hanjin Yoo[8], Ki-Joon Jeon [9] & Weijun Li [1] ✉

Black carbon (BC) aerosols, with their strong light-absorbing ability, are major drivers of the global climate. In existing models, BC aerosols are simplified as a single core when determining radiative effects. Here, we found that 21% of BC aerosols contain multiple cores during a wildfire smoke observation. By considering dynamic effective medium approximation (DEMA) with Mie theory and assuming randomly distributed multi–core BC, the light absorption was 1.81 times greater than that under the single–core assumption for particles with overall diameters >400 nm and core diameters >200 nm. A machine learning emulator was developed for DEMA-based absorption enhancements and incorporated into a global atmospheric model. For global aerosol absorption, multi–core BC particles lead to a 19% increase, especially in wildfire-affected regions. This study emphasizes the critical role of multi–core BC particles in amplifying radiative forcing and the necessity to revise models for the simulation of BC climate impact.

Black carbon (BC) plays a uniquely critical role in shaping the Earth's climate system through its radiative absorption ability and aerosol–cloud interactions, which allow it to contribute to slow winds[1], suppress the planetary boundary layer[2], alter snow and ice melting conditions[3], and generate other regional climate and weather changes[4,5]. Between 25 and 36% of global BC emissions originates from wildfires[6,7], with the remainder originating primarily from energy-related combustion processes, such as those associated with residential solid fuels and fossil fuels[6,8]. The intensity and duration of wildfires are increasing globally due to the higher temperatures, drier vegetation, and longer dry seasons resulting from climate change[5,9]. When BC

aerosols are coated by other nonabsorbing substances, the resulting lensing effect can significantly amplify their degree of light absorption, as quantified by the absorption enhancement factor, E_{abs}[10–13]. The Core–Shell Mie model, which is widely employed in atmospheric models (e.g., the Weather Research and Forecasting model coupled with Chemistry) can be used to obtain the light absorption enhancement (E_{abs_CS}) value of BC. In the Core–Shell Mie model, it is assumed that there is one central BC core per particle ($n_{core} = 1$)[14,15], and the BC mixing state is represented via the BC core diameter (D_c) and the particle-to-core diameter ratio (D_p/D_c). The total BC absorption level is represented by the black carbon absorption aerosol optical depth (BC

[1]State Key Laboratory of Ocean Sensing and Department of Atmospheric Sciences, School of Earth Sciences, Zhejiang University, Hangzhou, China. [2]Department of Science and Environmental Studies, The Education University of Hong Kong, Hong Kong, China. [3]Key Laboratory of Aerosol Chemistry and Physics and State Key Laboratory of Loess and Quaternary Geology, Institute of Earth Environment, Chinese Academy of Science, Xi'an, China. [4]Graduate School of Environmental Studies, Nagoya University, Nagoya, Japan. [5]Department of Civil and Environmental Engineering, Stanford University, Stanford, CA, USA. [6]Department of Earth and Planetary Sciences, Weizmann Institute of Science, Rehovot, Israel. [7]School of Geography, Earth and Environmental Sciences, University of Birmingham, Birmingham, UK. [8]Particle Pollution Research and Management Centre, Inha University, Incheon, Republic of Korea. [9]Department of Environmental Engineering, Inha University, Incheon, Republic of Korea. ✉e-mail: liweijun@zju.edu.cn

AAOD; Methods), which depends on both E_{abs} and the BC mass in the atmospheric column[16–18]. On the basis of the third phase of the Aerosol Comparisons between Observations and Models intercomparison initiative (AeroCom), BC AAOD accounts for 36%–84% of the global annual mean of total absorption aerosol optical depth (AAOD) at the 550-nm wavelength, indicating that BC yields a relatively notable warming effect[16–18]. However, AeroCom and other global observations indicated that global models frequently underestimate BC AAOD, and a scaling factor of 1.4–2.8 is needed to ensure alignment with global observational data for subsequent radiation assessment[6,17–19]. A quantitative review of the BC AAOD is provided in Supplementary Text 1. Some model studies attributed this upscaling factor to uncertainties in emission inventories and BC mass loads; moreover, these researchers focused on constraining the representation of the mixing state of BC in global atmospheric models[6,16,19].

Significant uncertainties exist in the mixing state and E_{abs} of BC in observations and simulations[11,13]. Fierce et al.[20] proposed that accounting for particle-to-particle heterogeneity in the mixing state and the complex morphology of BC-containing particles may resolve these uncertainties. Moreover, Liu et al.[10] and Fierce et al.[20] reported that the Core–Shell Mie model might oversimplify the nonspherical morphology of BC particles, leading to potential overestimation of the degree of light absorption at low D_p/D_c values (<-1.4). Chen et al.[21] further proposed that nonsphericity contributes only marginally (3.3%) to the global BC AAOD. In field studies, researchers reported E_{abs_CS} values varying between 1 and -1.5; these studies relied solely on single particle soot photometers (SP2) and obtained E_{abs_CS} values via the Core–Shell Mie model[22,23]. Direct optical measurements conducted with a photoacoustic spectrometer, a particle soot absorption photometer, and other technologies were employed to determine the average E_{abs} values, which ranges from 1 to -2.5[20,24] (refer to Supplementary Table 1 for details). It is well known that SP2 measurements and laboratory experiments typically exhibit an upper size limit of $D_p <$ -400 nm, with the detailed range depending on the SP2 configuration[25,26]. However, field studies roughly estimated that the contribution of BC-containing particles with $D_p > 400$ nm to the bulk BC mass and light absorption level could reach 50%, especially during polluted periods[27,28]. Detailed comparisons of D_p and D_c across model, field, and laboratory studies are summarized in Supplementary Text 2 and Supplementary Table 2. These findings highlight a gap in the understanding of how the mixing state of large particles ($D_p > 400$ nm) affects E_{abs}.

Our study is further inspired by considering the maximum E_{abs} value of -4, which was reported in certain experiments and field studies[29–32] and is consistent with the simulations of Fuller, et al.[33]. Importantly, the simulations by Fuller, et al.[33] were based on the Dynamic Effective Medium Approximation (DEMA) with Mie theory under the assumption that multiple BC cores ($n_{core} \geq 1$) are randomly distributed within particles[33–36]. However, the impacts on E_{abs} and BC AAOD have been neglected because of a lack of direct evidence for $n_{core} > 1$ in DEMA for ambient BC particles. Transmission electron microscopy (TEM) enables detailed analysis of individual particles, and this technique effectively captures the mixing structure of BC-containing particles[15,37]. Multi–core BC particles have occasionally been reported in previous studies on the basis of TEM (refer to Supplementary Table 3 for details), but their roles in driving radiative forcing and their connection to DEMA remain underexplored. One recent study confirmed that coagulation leads to the occurrence of multi–core BC particles with $D_p > 400$ nm during long-range transport[38]. Some field studies have proposed that coagulation during the long-range transport of wildfire smoke drives the increase in the D_p value of BC-containing particles[39–42]. Satellite observations show that wildfire smoke produces a dense haze layer at 2000–4000 m above sea level (a.s.l.) from Southeast Asia to Yunnan Province, China[4,43]. Therefore, these wildfire events provide unique real-world

laboratory setting for understanding BC light absorption and the changes in mixing states during transport, particularly for multi–core BC aerosols.

To characterize the evolution of mixing states for transported BC, we conducted a field campaign at the Yunya Atmospheric Environment Research Observatory (YAREO) during the wildfire-affected periods. The station is located atop a mountain in Yunnan Province at 2200 m a.s.l. (Fig. 1). We quantified the impact of n_{core} on the size dependence of E_{abs} and the subsequent influence on BC AAOD with machine learning algorithms in a global atmospheric model. This study provides the insight into addressing the missing absorption enhancement resulting from multi–core BC aerosols in global atmospheric models.

Results and Discussion
Characteristics of aerosol particles
Highly polluted periods are defined as when the total mass of elemental carbon, organic matter, dust, and water-soluble inorganic ions exceeds 15 µg m^{-3} at the sample station (Supplementary Fig. 1). We found that mass concentrations of these aerosol chemical components during highly polluted periods were approximately 3 times higher than them during less polluted periods (e.g., elemental carbon in Supplementary Table 4). In Supplementary Fig. 2a, BC concentrations increased from 0.15 to 4.4 µg m^{-3} over the sampling period, driving BC AAOD to increase from 0.003 to 0.062 based on Modern-Era Retrospective analysis for Research and Applications version 2 (MERRA2). Additionally, Supplementary Fig. 2b-d show that regional BC concentration and BC AAOD during highly polluted periods were about three times higher than them during less polluted periods, while PM$_{10}$ concentration at the downstream national monitoring station became double during highly polluted periods. Satellite data and air mass trajectories both indicated that south-westerly air masses passed over areas with intense fire activity in Southeast Asia during highly polluted periods, leading to regional pollution events at the downwind sampling site (Fig. 1a). In contrast, western trajectories from South Asia rarely passed over fire-affected regions during less polluted periods (Supplementary Fig. 3). These results suggested that the highly polluted periods were influenced mainly by the long-range transport of wildfire smoke from Southeast Asia, providing ideal real-world conditions for understanding BC ageing mechanisms during long-range transport.

In TEM images, BC particles appeared as fractal-like aggregates of soot, and they were either externally mixed as bare-like BC aerosols (Fig. 1b1) or BC aerosols coated with secondary aerosols (Fig. 1(b2–b3)) after undergoing ageing processes, such as condensation, coagulation, and cloud processing[15,25]. Among the 3950 analysed particles, 47% were BC-containing particles, comprising 33% coated BC particles and 14% bare-like BC particles (Fig. 1c), whereas the remainder were BC-free particles (Supplementary Fig. 4). In summary, multi–core BC particles accounted for 21% of the BC-containing particles, 14% during the less polluted periods and 25% during the highly polluted periods (Fig. 1c). The detailed individual-particle analysis can be found in the Methods section and Supplementary Text 3.

During highly polluted periods, wildfire smoke after long-range transport could enhance the formation of multi–core BC particles (Fig. 1a vs. Supplementary Fig. 3). However, few studies reported the size-dependent characteristics of multi–core BC particles. Instead, some studies considered the two-dimensional data characteristics of D_p/D_c and D_c and the size distribution of D_c to approximately assess the mixing states of BC aerosols in biomass burning smoke and wildfire smoke[26,44,45]. To obtain the equivalent volume diameters of individual BC-containing particles and their BC cores (i.e., D_p and D_c, respectively), we calibrated the equivalent circle diameters obtained from TEM images to the equivalent volume diameters via a regression relationship from atomic force microscopy measurements (refer to the Methods). For multi–core BC particles,
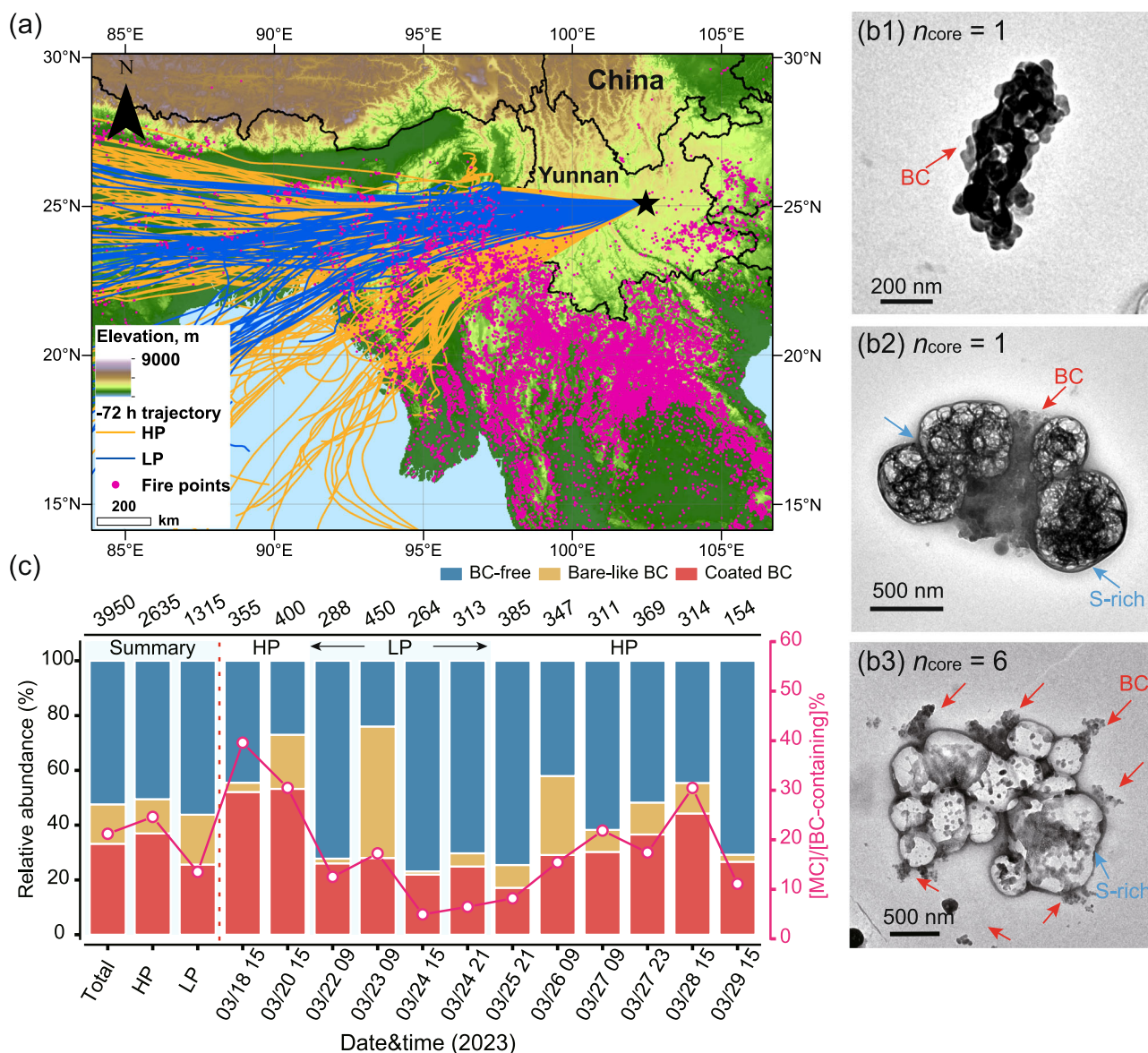
Fig. 1 | Individual particle analysis at Yunya mountain station in Yunnan province of China. a 72-h backward trajectories arriving at 2000 m above ground level during the sampling periods (March 18-29, 2023), including highly polluted (HP) and less polluted (LP) periods. **b1–b3** Transmission electron microscopy (TEM) images of particles containing different number of black carbon (BC) cores (n_{core}). **c** Relative abundance of different particle types and the proportion of multi–core BC particles (MC, $n_{core} > 1$) to all BC-containing particles. "Total", "HP", and "LP" represent the summary results during the whole periods, highly polluted periods, and less polluted periods, respectively.

D_c represents the diameter of a single sphere whose volume is equivalent to the sum of all BC core volumes. Figure 2a and Table 1 both show that multi–core BC particles became the dominant particle type at $D_c > 200$ nm.

Figure 2b shows that the average D_p/D_c ratio first decreased with increasing D_c, and then remained relatively constant for particles with $D_c > 200$ nm. This relationship was well fitted by the following equation: $D_p/D_c = 2.5 + 6.3 \times Exp(-D_c/63)$ (purple line in Fig. 2b). The fitting results revealed that the average D_p/D_c ratio remained steady at 2.5, mainly for $D_p > 400$ nm (blue and green dots in Fig. 2b). Similar plateau values of D_p/D_c were reported for Southeast Tibetan Plateau (~ 2.2)[38] and during a transboundary transport event in Beijing (~ 2.4)[44]. If condensation dominated the BC aging mechanism ($n_{core} = 1$), particles with smaller D_c values would exhibit higher D_p/D_c values when coated with the same volume of condensate aerosols[25]. Specifically, D_p/D_c was expected to approach ~1 with increasing D_c value. The blue line shown in Fig. 2b represents the maximum D_p/D_c

value under the condensation mechanism described by Chen et al.[38] and Sedlacek et al.[25]. Figure 2b shows that particles with $D_p > 400$ nm (blue and green dots) were above the blue line. Below this blue line, condensation dominated the BC ageing process, maintaining the n_{core} value at 1 (Fig. 2c). Above the blue line, coagulation dominated the ageing process, resulting in an increase in the n_{core} value (i.e., $n_{core} > 1$) (Fig. 2c).

Box models developed by Matsui et al.[46] and Riemer et al.[47] revealed that thickly coated BC particles were dominated by coagulation rather than by condensation. They concluded that the number of coagulation events increased with increasing D_p and peaked at $D_p > ~400$ nm[46]. Several field studies proposed that coagulation could account for most of the increase in particle size (D_p) in wildfire smoke[39–42]. Theoretically, coagulation between two BC-containing particles could increase n_{core} and produce a larger D_c value[46]. In this study, multi–core BC particles were observed in the TEM images (Fig. 1b3), thus providing direct evidence of coagulation among
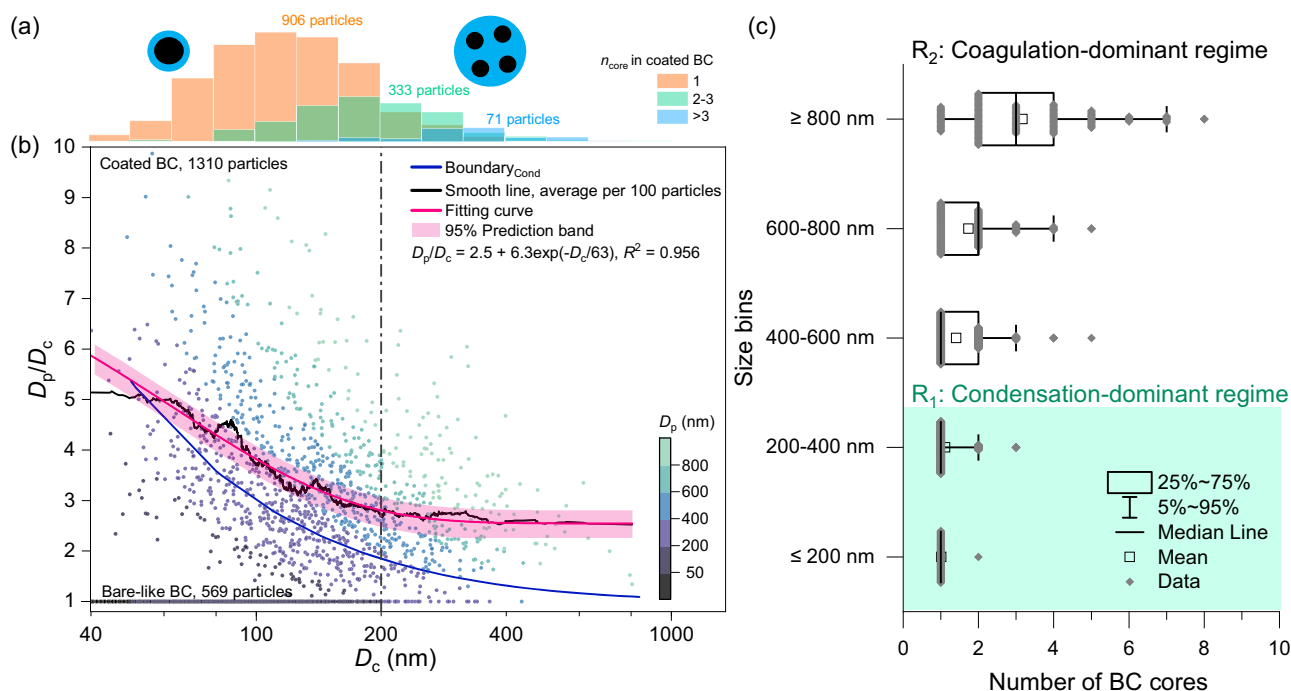
Fig. 2 | Quantifying the size-dependence characteristics of black carbon (BC) mixing state. a Different colours represent the number of BC cores (n_{core}) in each particle, and the histogram is the number distribution of particles with different BC core size (D_c). D_c is the cumulative equivalent volume diameter of all BC cores in a particle. **b** Two-dimension distribution of particle-to-core diameter ratio (D_p/D_c) and D_c based on the transmission electron microscopy. The smooth line is used for all coated BC particles (black) and their fitting curve (purple). The Boundary$_{cond}$ line means the max D_p/D_c versus D_c via the condensation processing, and beyond Boundary$_{cond}$ line, changes in D_p/D_c are predominantly influenced by coagulation. The Boundary$_{cond}$ line is well described in Chen et al.[38] and Sedlacek et al.[25]. **c** The range of n_{core} in different size bins based on the diameter of the whole particle (D_p).

Table 1 | Comparison of particles containing the different number of black carbon cores (n_{core})

Particle number fraction [a]		Type based on n_{core}		
		$n_{core} = 1$	$n_{core} > 1$	Sum
Type based on different proxy features	M_1[b]: $D_c > 200$ nm			
	0	62%	15%	100%
	1	7%	16%	
	M_2[b]: $D_p > 400$ nm			
	0	39%	4%	100%
	1	30%	27%	
	$M_1 \times M_2$[b]			
	0	64%	16%	100%
	1	5%	15%	

[a] For a total of 1310 coated black carbon (BC) particles;
[b] M_1 represents whether the cumulative equivalent volume diameter of all BC cores in a particle (D_c) is larger than 200 nm. If so, the value is 1; otherwise, it is 0. M_2 represents whether the diameter of the whole particle (D_p) is larger than 400 nm. If so, the value is 1; otherwise, it is 0. Only when M_1 and M_2 meet both conditions is $M_1 \times M_2 = 1$.

BC-containing particles. Figure 2c shows that the range of n_{core} increased with increasing D_p: for example, n_{core} ranged from 1 to 5 for D_p between 400 and 600 nm, and from 1 to 8 for $D_p \geq 800$ nm. We observed a critical condition near $D_p > 400$ nm and when n_{core} transitioned from 1 to >1 (Fig. 2c). This phenomenon was also observed in the Southeast Tibetan Plateau[38] and Amakusa City, Japan[48]. Table 1 indicates that multi-core BC particles became the dominant type of coated BC particles for $D_p > 400$ nm and $D_c > 200$ nm. To facilitate parameterization, we defined two proxy features (M_1 and M_2), as expressed in Eq. (1), to represent the primary size characteristics of multi-core BC particles and their subsequent impact on E_{abs}. In 1310 coated-BC particles, 20% simultaneously satisfied $M_1 = 1$ and $M_2 = 1$ (i.e., $M_1 \times M_2 = 1$), in which the number of multi-core BC particles was three times greater than that of single-core BC particles (Table 1).

$$M_1 = \begin{cases} 0 & D_c \leq 200 \\ 1 & D_c > 200 \end{cases} \quad M_2 = \begin{cases} 0 & D_p \leq 400 \\ 1 & D_p > 400 \end{cases} \quad (1)$$

Optical absorption enhancement

In this study, we employed an electron-microscopy-to-BC simulation tool, coupled with discrete dipole approximation (EMBS-DDA)[37] to visualize the effect of n_{core} on E_{abs} of BC-containing particles. The EMBS tool provides an interactive interface for designs of particles with different sizes and positions of cores that are input into the DDA module to calculate their optical properties[37]. To explain the differences between single-core and multi-core BC particles, we further adopted the near-field calculation algorithm of DDA[49–51] to simulate the light electric field intensity inside and around scattering particles (i.e., secondary aerosols) and coated BC particles, respectively.

BC-containing particles were assigned different n_{core} values and positions in the EMBS-DDA simulations, whereas D_p/D_c was set to the average value (i.e., $D_p/D_c = 3$ in Supplementary Fig. 5) to represent the common scenario for $D_p > 400$ nm. Under the assumption that BC cores were randomly located in an individual particle, the probability of core occurrence obviously increased from the centre to off-centre positions. Specifically, BC aerosols with a single core or multiple cores at the particle centre represented idealized and specialized scenarios, respectively. Innumerable possible core locations would increase the DDA simulation burden of every configuration excessively, even with fixed input parameters of D_p, D_c, and n_{core}. Herein, we simulated three representative scenarios using DDA:

DDA$_1$: Setting $n_{core} = 1$ with the core at the centre. The simulated E_{abs} value was almost equal to that of the Core–Shell Mie model, as shown in Fig. 3a–b.
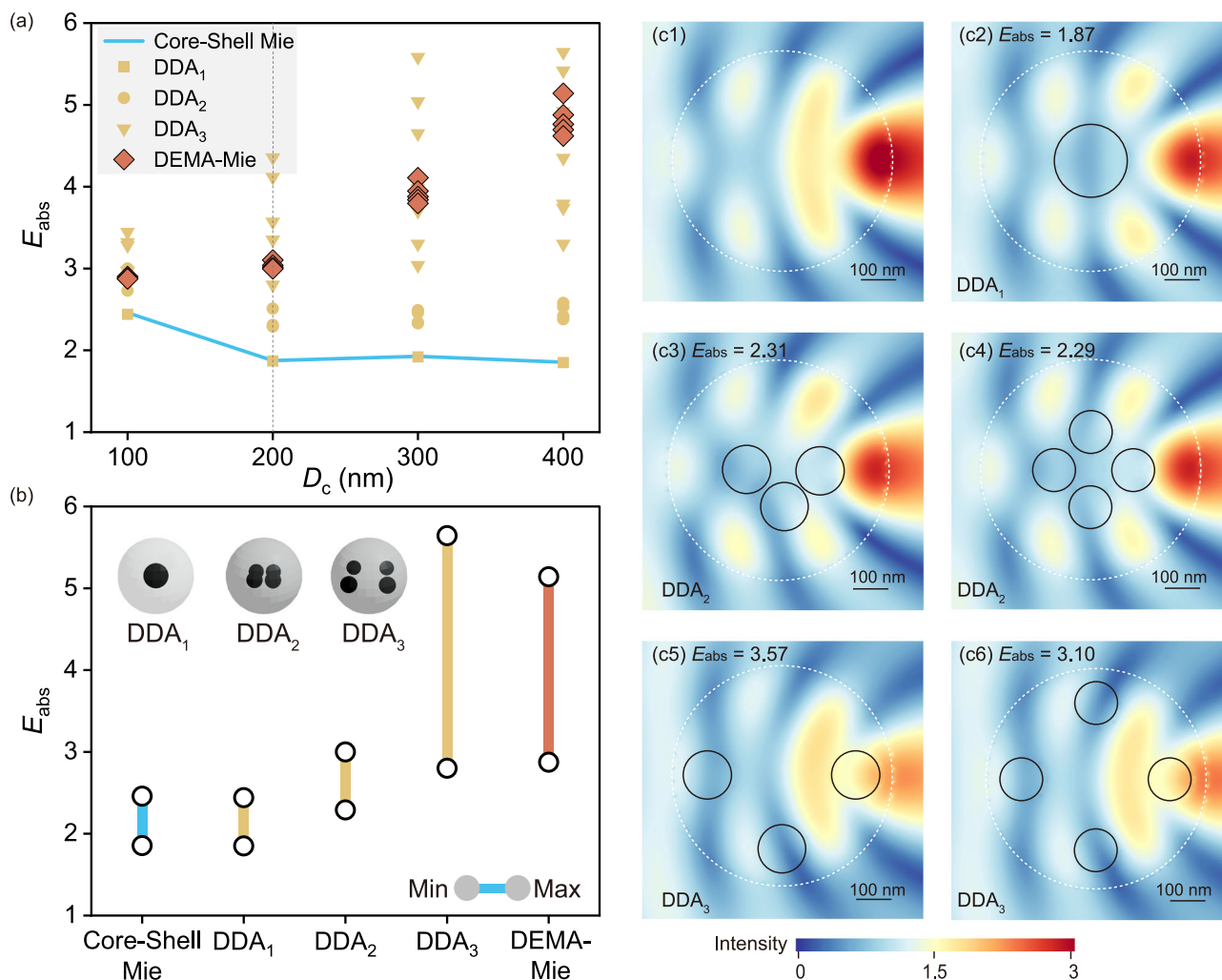
Fig. 3 | Light absorption enhancement (E_{abs}) at 550 nm of different types of black carbon (BC) containing particles. a Simulation results of different methods for different diameters of BC cores (D_c). D_c is the cumulative equivalent volume diameter of all BC cores in a particle. Input parameters and simulation outputs are detailed in Supplementary Tables 5 and 6. **b** Schematic diagrams illustrate typical mixing states for different discrete dipole approximation simulations (DDA$_1$, DDA$_2$, and DDA$_3$), each with distinct core configurations. **c1–c6** Near-field calculations were employed to determine the electric field intensity at 550 nm for secondary aerosol particles (**c1**) and various DDA scenarios (DDA$_1$: **c2**, DDA$_2$: **c3-4**, DDA$_3$: **c5-6**), with the diameter of the whole particle (D_p) at 600 nm. Supplementary Fig. 9 also provides simulation results for $D_p = 300$ nm. White lines represent the border of particles, and black line marks the location of the BC cores. The colour represents the normalized electric field intensity versus the incident light (dimensionless).

DDA$_2$: Setting $n_{core} > 1$ with multiple cores concentrated near the centre, as shown in Fig. 3b.

DDA$_3$: Setting $n_{core} > 1$ with cores distributed at various off-centre positions, as shown in Fig. 3b. The detailed settings are provided in Supplementary Text 4, Supplementary Tables 5–6, and Supplementary Fig. 6. In addition, we calculated E_{abs} via the Core–Shell Mie and DEMA–Mie models on the basis of the same input parameters (D_p, D_c, and n_{core}) used in DDA. Each core is the same size in the particles in DDA$_1$-DDA$_3$, and Supplementary Fig. 7 shows the simulations with different sizes of BC cores (Diff. Size). In Supplementary Fig. 7, Diff. Size shows a similar range of E_{abs} with DDA$_1$-DDA$_3$, which supports the assumption in Jacobson[52]: it is ideal to track a size distribution of BC within coated BC particles of each size, but a monodisperse distribution of BC within coated particles was used for quick optical simulations.

We found that the E_{abs} values for $n_{core} = 1$ were 12–222% lower than those for $n_{core} > 1$, particularly in DDA$_3$ scenarios (Supplementary Table 6). Figure 3a shows that the DEMA–Mie could represent the average increasing trend in DDA$_3$. Notably, the DEMA–Mie model accounted for scenarios with $n_{core} \geq 1$ in which the cores were randomly distributed, but their exact locations were not specified in DDA. We compared the E_{abs} ranges (from minimum to maximum) obtained via the DEMA–Mie and DDA$_3$ simulations. Figure 3b shows that the E_{abs} range from the DDA$_3$ simulations agreed well with that from the DEMA–Mie model. The results further confirmed that DEMA–Mie was efficient for simulating the average impact of n_{core} at random positions on E_{abs}.

Supplementary Fig. 8 shows that the light electric field intensity was enhanced (lensing effect) in the off-centre region of a secondary scattering particle, which is consistent with the experiment findings of Arroyo, et al.[50] and Li, et al.[53]. The intensity of the enhanced field, as indicated by colour, was particularly high for $D_p > 400$ nm (Supplementary Fig. 8). We further modelled the electric field intensity for coated BC particles with various n_{core} values, as shown in Fig. 3(c1–c6) for $D_p = 600$ nm and Supplementary Fig. 9 for $D_p = 300$ nm. Figure 3(c1–c6) show the enhanced presence of white and orange areas in the regions marked by black circles, suggesting that DDA$_2$ and DDA$_3$ exhibited higher E_{abs} values than did the DDA$_1$ simulations. In
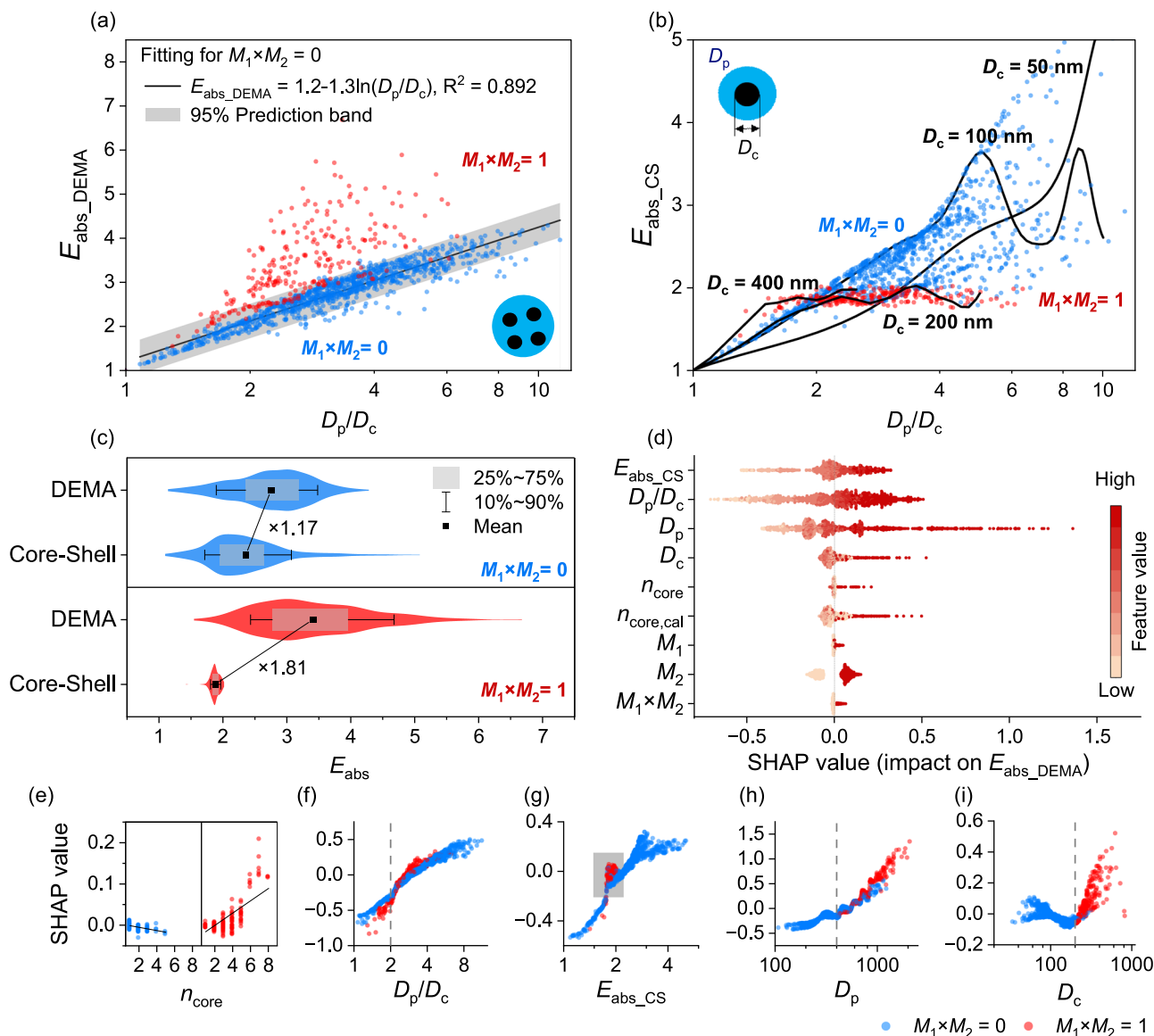
Fig. 4 | Random Forest Model Emulation of Light Absorption Enhancement (E_{abs}) **at 550 nm.** $M_1 \times M_2 = 1$ represents the particles with the diameter of black carbon (BC) cores (D_c) larger than 200 nm and the diameter of the whole particle (D_p) larger than 400 nm. D_c is the cumulative equivalent volume diameter of all BC cores in a particle. **a** Fitting of E_{abs_DEMA} for particles with $M_1 \times M_2 = 0$ (blue points) using the dynamic effective medium approximation with Mie model (DEMA–Mie). **b** Lines showing the increase in E_{abs} as the particle-to-core diameter ratio (D_p/D_c)

increases across various D_c values under the Core–Shell Mie model (E_{abs_CS}). **c** Comparison analysis of differences between E_{abs_DEMA} and E_{abs_CS} for $M_1 \times M_2 = 0$ and 1, respectively. **d** Impacts on E_{abs_DEMA} shown as different SHAP values for each input feature via SHapley Additive ExPlanation (SHAP) approach. Further details on SHAP are in the Methods section. **e–i** Impacts of primary input features on E_{abs_DEMA} quantified by the SHAP values.

Supplementary Fig. 9, a smaller colour gradient indicates a weaker lensing effect for $D_p = 300$ nm, but the difference in E_{abs} between Core-Shell structure and multi-core structure is still up to 1 (DDA$_1$ vs. DDA$_3$). Kahnert et al.[54] also proposed that the energy field rapidly attenuated within a solid BC sphere, which limits the contribution of the core mass near the particle centre to light absorption. Moreover, Beeler and Chakrabarty[55] defined a phase shift parameter to describe a simulation like Fig. 3c2. However, in these previous simulations, multi–core BC particles were not employed as input parameters.

E_{abs_DEMA} exhibited a quasilinear increase with the logarithm of D_p/D_c under $M_1 \times M_2 = 0$ for all 1310 coated BC particles (black line in Fig. 4a). Notably, the particles with $M_1 \times M_2 = 1$ (red dots in Fig. 4a) exhibited higher E_{abs_DEMA} values than did those with $M_1 \times M_2 = 0$ (blue dots) for the same D_p/D_c value. In contrast, the Core–Shell Mie model showed that E_{abs_CS} first increased with increasing D_p/D_c and then

plateaued at ~2 for $M_1 \times M_2 = 1$ (red dots in Fig. 4b). The differences between E_{abs_DEMA} and E_{abs_CS} indicated that E_{abs_DEMA} was 1.17 and 1.81 times greater than E_{abs_CS} for $M_1 \times M_2 = 0$ and 1, respectively (Fig. 4c).

In summary, these findings suggested that the Core–Shell Mie model could significantly underestimate the light absorption of BC-containing particles when $M_1 \times M_2 = 1$. However, the DEMA–Mie model could be a suitable and efficient tool for simulating the optical properties of multi–core BC particles. Therefore, the developed DEMA–Mie model provides a more favourable balance between computational efficiency and physical representation than the DDA and Core–Shell Mie models.

Machine learning emulator

In previous global simulations, the developers of DEMA[52,56,57] used a noninteger $n_{core,cal}$ value (i.e., $D_c^3/1,000,000$) to approximate n_{core}.

However, Wang, et al.[58] proposed that a noninteger $n_{core,cal}$ value was implausible because observational evidence for multi–core BC particles was lacking. Therefore, it was necessary to parameterize the impact of n_{core} on E_{abs} on the basis of the real-world size dependence of n_{core}. We employed a random forest (RF) model to predict E_{abs_DEMA} and quantify how E_{abs_DEMA} changed with the mixing state of coated BC. On the basis of 1310 samples (coated BC particles), we developed two RF emulators (RF1 and RF2) for E_{abs_DEMA}, with input features including D_p/D_c, D_c, D_p, E_{abs_CS}, n_{core}, $n_{core,cal}$, M_1, M_2, and $M_1 \times M_2$. RF1 included all the input features, whereas RF2 excluded n_{core}, which was generally unavailable in global models. SHapley Additive ExPlanation (SHAP) values, rooted in coalitional game theory[59], were employed to distribute the total effect of each input feature on the predicted E_{abs_DEMA} for individual particles (refer to the Methods). By comparing the prediction performance levels and SHAP values of RF1 and RF2, we determined whether $M_1 \times M_2$ could serve as a proxy for the impact of n_{core} on E_{abs_DEMA}.

RF1 performed well for both the training and test datasets, achieving an R^2 value of 0.96 (Supplementary Fig. 10 and Supplementary Table 7). Figure 4d shows that D_p/D_c, D_c, D_p, and E_{abs_CS} were the primary driving features due to their broad SHAP value distributions. Notably, the SHAP distributions for n_{core} and $M_1 \times M_2$ exhibited a T shape, indicating that there was a threshold effect on E_{abs_DEMA} (Fig. 4d). To enhance the interpretability of the RF predictions, we visualized the SHAP values corresponding to each feature value. Figure 4(e–i) show the driving patterns of these primary features on E_{abs_DEMA}. Each point represents an individual particle, and its colour is indicative of its $M_1 \times M_2$ value to illustrate how $M_1 \times M_2$ influences the driving patterns of these features (Fig. 4e–i). Figure 4e shows that n_{core} was positively correlated with its SHAP values only when $M_1 \times M_2 = 1$; otherwise, the SHAP values were approximately 0. These results suggested that the impact of n_{core} on E_{abs_DEMA} was the most significant for particles with $M_1 \times M_2 = 1$. Figure 4f shows a positive correlation between D_p/D_c and its SHAP value, with a steeper trend for particles with $M_1 \times M_2 = 1$ (red) that that of particles with $M_1 \times M_2 = 0$ (blue). This result indicated a greater increase in E_{abs_DEMA} with increasing D_p/D_c for $M_1 \times M_2 = 1$. Figure 4g shows that E_{abs_CS} positively correlated with its SHAP value overall, except for particles within the grey-shaded region where $E_{abs\_CS} \approx 2$. For these particles, the SHAP value was close to zero when $M_1 \times M_2 = 1$ (red in Fig. 4g), suggesting that E_{abs_CS} had predictive utility for E_{abs_DEMA} for $M_1 \times M_2 = 0$ but not for $M_1 \times M_2 = 1$. The increasing D_p value led to a greater increase in E_{abs_DEMA} with $M_1 \times M_2 = 1$ (Fig. 4h), whereas the transition of $M_1 \times M_2$ from 0 to 1 altered the correlation of D_c with its SHAP value from negative to positive (Fig. 4i). These findings suggested that D_p and D_c exerted a nonlinear driving effect on E_{abs_DEMA} and that BC cores with $M_1 \times M_2 = 1$ exhibited more notable interactions with light. Similar patterns were observed when n_{core} (Supplementary Fig. 11) was used to explain the driving patterns in RF1 compared with when $M_1 \times M_2$ was used, as shown in Fig. 4(f–i). We concluded that $M_1 \times M_2$ could serve as a proxy for the impact of n_{core} on E_{abs_DEMA}.

To assess the predictive performance of E_{abs_DEMA} without n_{core} as an input feature, we performed additional tests to construct RF2. In RF2, the input features included D_p/D_c, D_c, D_p, E_{abs_CS}, $n_{core,cal}$, M_1, M_2, and $M_1 \times M_2$. RF2 performed comparably to RF1, achieving an R^2 value of 0.95 (vs. 0.96 for RF1) and a root mean square error (RMSE) of 0.14 (vs. 0.17 for RF1) (Supplementary Table 7). The SHAP value distributions remained consistent between RF1 and RF2 (Supplementary Fig. 12 vs. Figure 4), further confirming that $M_1 \times M_2$ could effectively replace n_{core} for predicting E_{abs_DEMA} in machine learning models.

Implications for the atmospheric model

Multi–core BC particles are not exclusive to wildfire smoke events but are instead widely observed in other environments, as listed in 11 additional studies in Supplementary Table 3. However, these studies
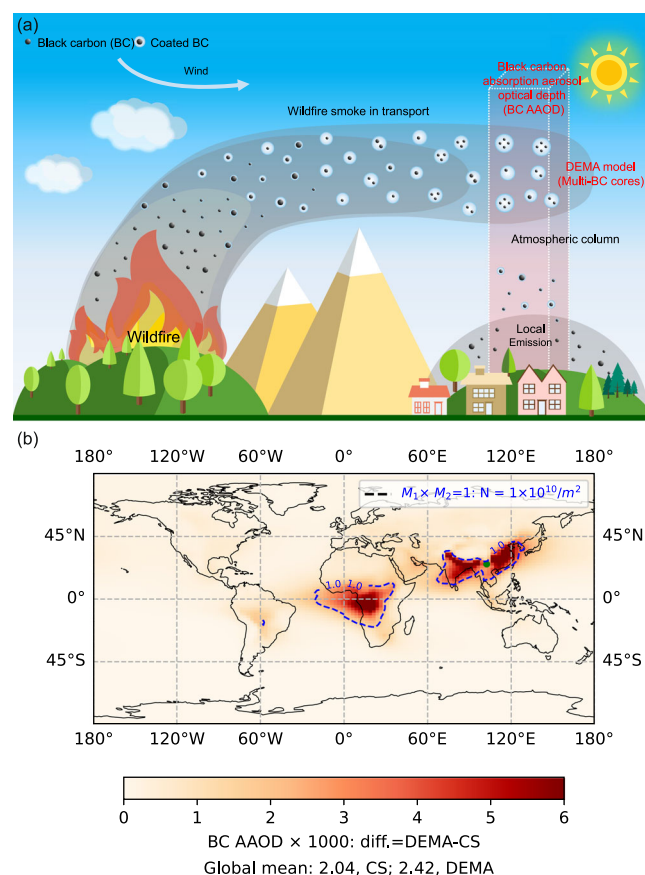
Fig. 5 | Global impact of multi–core black carbon (BC) particles on black carbon absorption aerosol optical depth (BC AAOD). a A conceptual scheme of wildfire smoke in transport. **b** Global distribution of annually average differences in BC AAOD using Core–Shell (CS) model and dynamic effective medium approximation (DEMA) with Mie theory (DEMA–Mie) respectively. Blue lines mark the area where the number concentration reaches 10^{10} m^{-2} for BC-containing particles with the diameter (D_p) larger than 400 nm and the diameter of BC cores (D_c) larger than 200 nm (i.e., $M_1 \times M_2 = 1$) in the atmospheric column. Green point is the sample station.

did not focus on multi–core particles or their optical properties. To evaluate the global impact of multi–core BC particles on the bulk optical properties of dry aerosols, we coupled the Community Atmosphere Model with the Aerosol Two-dimensional bin module for foRmation and Aging Simulation (CAM–ATRAS, a global model) and the RF2 model offline (refer to the Methods and Supplementary Fig. 13). CAM–ATRAS model showed that wildfire sources dominated BC sources in regions such as South Africa and South America (Supplementary Figs. 14a–c). The long-range transport of wildfire emissions from Southeast Asia to southern China frequently increased the BC loadings in March (Supplementary Figs. 14d–e). The global distribution of particles with $M_1 \times M_2 = 1$ overlapped with wildfire hotspots (Supplementary Figs. 15a–e) and regions of intensive anthropogenic emissions (Supplementary Figs. 15f–g). In these areas and downstream regions, such as oceans and the Tibetan Plateau, particles with $M_1 \times M_2 = 1$ accounted for ~2% of the total number and ~30% of the mass of BC in the atmospheric column (Fig. 5a and Supplementary Figs. 16–17). Figure 5b shows that the global average BC AAOD was 2.04×10^{-3} under the Core–Shell Mie model but increased to 2.42×10^{-3} under the DEMA–Mie model. These large differences occurred mainly in high-emission regions such as China, India, and South Africa, where the elevated BC AAOD was driven by the number concentrations ($N_{M1 \times M2 = 1}$) of particles with $M_1 \times M_2 = 1$ in the atmospheric column

(Supplementary Fig. 18 and the blue contours in Fig. 5b). Furthermore, the relative difference in the BC AAOD was 19% globally. Hot spots (>19%, red colour in Supplementary Fig. 19) were located downstream of high-emission regions, due to the higher fraction of particles with $M_1 \times M_2 = 1$ (Supplementary Figs. 16-17), which highlighted the role of transported aerosols in determining the BC AAOD.

We highlighted the enhanced light absorption due to multi–core BC particles and acknowledged the potential overestimation of E_{abs} simulations due to the nonsphericity of BC particles at low D_p/D_c values[10,20]. In their experiment, Liu et al.[10] measured a value of E_{abs} near 1 for $D_p/D_c < 1.4$, whereas the calculated E_{abs_CS} value increased with increasing D_p/D_c. Our study could address the gap in that of Liu et al.[10], where E_{abs} and the mixing state were clearly marked as unknown for $D_p/D_c > 3$ owing to the upper measurement limit of the SP2 instrument (i.e., $D_c < \sim 400$ nm). We conducted a sensitivity analysis by setting E_{abs} at 1 for $D_p/D_c < 1.4$ and using RF2 in CAM–ATRAS to compare the relative importance due to nonsphericity and multi–core nature of BC particles. We defined a ratio between the DEMA-derived increase and the nonsphericity-derived decrease in the global BC AAOD (refer to the Methods). According to Supplementary Fig. 20, this ratio could increase by up to fourfold across the downstream areas of high-emission regions, particularly in wildfire areas such as Southeast Asia and the sample station of this study.

We evaluated the impacts of multi–core BC particles in dry aerosol particles by using a real-world n_{core} value rather than the assumed $n_{core,cal}$ value, integrating microscale individual-particle analysis with optical simulations and global models. BC-containing particles could be activated into cloud condensation nuclei when the humidity increases[15,60]. Via a rough estimation that involved replacing n_{core} with $n_{core,cal}$ for individual cloud droplets, Jacobson[35,52] reported that the DEMA–Mie model could yield a greater near-surface temperature increase (+33%), greater heating rate (+130%), and a larger number of interstitial aerosol particles (+140%), compared to the Core–Shell Mie model. However, accurately parameterizing the changes in n_{core} during aerosol–cloud interactions remains a significant challenge, particularly during long-range transport and cloud processes. Therefore, we propose that future global and regional models should incorporate multi–core BC scenarios, potentially for particles with $D_p > 400$ nm and $D_c > 200$ nm, to increase the accuracies of BC light absorption and radiative forcing predictions. Our study highlights the missing absorption enhancement of multi–core BC aerosols in ambient air, which helps improve the atmospheric modelling of these aerosols and their potential climatic impacts.

Methods

Aerosol collection and measurement

Aerosol samples were collected from 18 to 29 March 2023 at the Yunya Atmospheric Environment Research Observatory station of the Chinese Academy of Science in Woyun Mountain, west of Kunming, Yunnan Province (25.16 N, 102.4 E, 2200 m a.s.l. in Fig. 1a). A KB-120F sampler with a flow rate of 100 L min^{-1} was used to collect PM$_{10}$ samples (particulate matter with an aerodynamic diameter ≤ 10 μm) on 90-mm-diameter quartz filters for 11.5 h (09:30–21:00 for the daytime; 21:30–09:00 for the nighttime in Beijing time). The chemical composition of PM$_{10}$ was analysed (refer to Supplementary Text 5 for more details). Hourly PM$_{10}$ data were downloaded from the China National Environmental Monitoring Centre (https://air.cnemc.cn: 18007/). MERRA2 provided the hourly mass concentrations of BC and the BC AAOD at 550 nm during the sampling periods (https://gmao.gsfc.nasa.gov/reanalysis/MERRA-2/).

Individual particle collection and morphological analysis

A portable DKL-2 sampler (Genstar Electronic Technology, China) equipped with a 0.5-mm jet nozzle was employed to collect individual aerosol particles. The particles were collected on a copper grid coated with a carbon film (carbon Type-B, 300-mesh copper; Tianld Co., China) and silicon wafers. These samples were collected at 3:00, 9:00, 15:00, and 21:00 Beijing time for 15–40 min and stored in plastic capsules under low relative humidity (RH = 20-25%). Twelve samples were selected, and a total of 3950 particles were analysed via TEM (JEOL JEM-2100, Japan) in combination with energy-dispersive X-ray spectroscopy (EDS; INCA X-Max^N 80 T, Oxford Instruments, United Kingdom). The strong electron beam of TEM could easily damage the coating of the coated BC particles[61]. Therefore, we determined the morphology and number of BC cores in an individual particle with this technique, as shown in Supplementary Fig. 21.

RADIUS software (EMSIS GmbH, Germany) was adopted to measure the morphological features of individual particles in the TEM images, e.g., the equivalent circle diameter (ECD) and bearing area (A). Additionally, individual particles on silicon wafers were measured via atomic force microscopy (AFM). Gwyddion 2.64 software (http://gwyddion.net/) was used to automatically obtain the bearing area (A) and bearing volume (V) of 165 individual particles. The ECD and equivalent volume diameter (EVD) of individual particles were calculated according to the following Eqs. (2–3)[48]:

$$A = \frac{1}{4}\pi(ECD)^2 \qquad (2)$$

$$V = \frac{1}{6}\pi(EVD)^3 \qquad (3)$$

where A is the bearing area, nm^2; V is the bearing volume, nm^3; ECD and EVD are the equivalent circle diameter and the equivalent volume diameter, nm, respectively.

A bootstrap linear regression analysis was used to obtain the transform ratio between the ECD and EVD. Through bootstrap analysis, we could use a limited dataset to estimate the slope coefficients in the regression equation by resampling 1000 times with replacement, which could increase the credibility and robustness of the results. The final equation was EVD = 0.54 × ECD, with an R^2 value of 0.99 (Supplementary Fig. 22). Consequently, a slope factor (k) of 0.54 was adopted to estimate the EVD from the ECD for all the particles in the TEM images. In this study, D_p was represented by the EVD of the whole particles (coating + BC cores). We used Eq. (4) to obtain D_c for all BC-containing particles.

$$D_c = \begin{cases} k \times ECD_{core} = k \times \sqrt[2]{\frac{4A_{core}}{\pi}} & n_{core} = 1 \\ k \times \sqrt[2]{\frac{4\sum_i^{n_{core}} A_{core,i}}{\pi}} & n_{core} > 1 \end{cases} \qquad (4)$$

where D_c is the cumulative equivalent volume diameter of all BC cores in a particle; n_{core} is the number of BC cores; the subscript i denotes the ith core; A_{core} is the bearing area obtained from the TEM images; k is the average transform ratio between the ECD and the EVD obtained via AFM, i.e., 0.54 as shown in Supplementary Fig. 22.

Light absorption enhancement (E_{abs})

In the DEMA–Mie model, it is assumed that one or multiple spherical BC cores are randomly distributed within one particle. The effective refractive index of the whole BC-containing particle (ϵ) could be obtained via Eq. (5)[34,62,63]. The Mie model was subsequently used to

calculate the optical properties at a wavelength of 550 nm.

$$\left(1 - \frac{D_c^3}{D_p^3}\right) \cdot \frac{\epsilon_{coat} - \epsilon}{\epsilon_{coat} + 2\epsilon} + \frac{D_c^3}{D_p^3} \cdot \frac{\epsilon_c - \epsilon}{\epsilon_c + 2\epsilon} + \frac{2\pi}{45}\left(\frac{2}{\lambda}\right)^2 \cdot (\epsilon_c - \epsilon) \cdot$$
$$\left[1 + \frac{5\epsilon}{2\epsilon_c + 3\epsilon} + \frac{18\epsilon(\epsilon_c - 2\epsilon)}{(\epsilon_c + 2\epsilon)^2}\right] \cdot \int r^5 n(r)dr = 0 \tag{5}$$

where r is the radius of a BC core, and $n(r)$ is the number concentration of cores per unit radius interval. The multi-BC cores cause complex light interactions and influence E_{abs}, which was considered as the third term in Eq. (5)[52,62]. Without the third term, Eq. (5) transforms into the Bruggeman mixing rule[34,52]. Owing to the lack of observational evidence for n_{core}, the developers of DEMA[52,56,57] used a noninteger $n_{core,cal}$ value (i.e., $D_c^3/1{,}000{,}000$) to approximate n_{core}. Individual particle analysis provided n_{core} values using TEM (e.g., $n_{core} = 6$ in Fig. 1b3). Notably, λ is the light wavelength, and we selected a value of 550 nm for one case. ϵ_c and ϵ_{coat} are the dielectric constants of BC and other aerosol components, respectively, which could be transformed via the widely used refractive index (RI) through the procedure outlined in Supplementary Text 6. According to the literature, the RI values are $1.85 + 0.71j$ for BC aerosols and $1.53 + 0j$ for coating aerosols[37,64]. Finally, the complex Eq. (5) was solved using the Newton–Raphson method, and the details are provided in Supplementary Text 6.

PyMieScatt, an open-source Python package, was used to calculate E_{abs} via Eq. (6), according to the Core–Shell Mie (E_{abs_CS}) and DEMA–Mie models (E_{abs_DEMA}), respectively[14,65].

$$E_{abs} = \frac{C_{abs,p}}{C_{abs,c}} \tag{6}$$

where $C_{abs,p}$ and $C_{abs,c}$ are the absorption cross sections of the coated BC particles and the bare BC particles, respectively. When the DEMA–Mie model is used, $C_{abs,c}$ is calculated for spherical BCs with the same D_c. To compare E_{abs_CS} and E_{abs_DEMA}, we applied EMBS–DDA model as a reference[37] and constructed different particle shapes with various D_c and n_{core} values at the same D_p/D_c. Details are provided in Supplementary Text 4.

Random forest (RF) and Shapley additive explanation (SHAP) approach

Both field and modelling studies face challenges in measuring and simulating n_{core} per particle[58]. Therefore, it is essential to quantify the potential nonlinear impact of n_{core} on E_{abs_DEMA} and to develop an emulator for E_{abs_DEMA} via the use of other features as proxies for n_{core}. We employed the RF model to create an emulator to predict E_{abs_DEMA}. We divided 1310 samples (coated BC particles) as follows: 70% were used for the training set, and 30% were used for the test set. Finally, two emulators were developed: RF1 included all input features, such as D_p/D_c, D_c, D_p, E_{abs_CS}, n_{core}, $n_{core,cal}$, M_1, M_2, and $M_1{\times}M_2$; RF2 excluded n_{core} and included other parameters. Furthermore, the SHAP approach was employed to distribute the total effect on the predicted E_{abs_DEMA} of each input feature[59]. According to coalitional game theory, the difference in model predictions involving a feature j (e.g., n_{core}) compared with the predictions without j was attributed to the marginal contribution of this feature. Considering the interactive effects between features, differences were computed for every possible feature subset combination of each sample[66]. For each particle sample, K features were input to generate the prediction for E_{abs_DEMA}, denoted

as $f(x_i)$, including a linear function of feature attribution in Eq. (7).

$$\begin{cases} f(x_i) = \Phi_0(f,x) + \sum_{j=1}^{K} \Phi_j(f,x_i) \\ SHAP(x_{i,j}) = \Phi_j(f,x_i) \\ \Phi_0(f,x) = \frac{\sum_i^N f(x_i)}{N} \end{cases} \tag{7}$$

where K is the total number of features; N is the total samples; $f(x_i)$ is the predicted E_{abs_DEMA} value for the ith particle via the RF model in this study; and $\Phi_j(f,x)$ is the SHAP value, which quantifies the impact of feature j on the prediction for input x_i in the built model. Specifically, the contribution of n_{core} (i.e., $j = n_{core}$) of the ith particle (x_i) to E_{abs_DEMA} was denoted the SHAP ($x_{i,j}$) value in Eq. (7), as shown by the scatter in Fig. 4e. The base value, $\Phi_0(f,x)$ was the average value of the predicted results. SHAP calculations were performed using the kernelshap and shapviz R packages, whereas the RF model was trained using the randomForest R package.

Parameterization and global model simulations

In many global models, accumulation-mode aerosols are over-simplified and represented by only a few mixing states[57,67]. As a result, BC-free particles are often misclassified as a coating on BC particles, leading to an 18–44% overestimation of the BC AAOD[21,57] (refer to Supplementary Text 1 for details). Although correcting this uncertainty is not our direct objective, we must ensure that BC-free particles do not confound our simulations and examination of the Core–Shell Mie and DEMA–Mie models. To address this issue, we selected the CAM–ATRAS, in which 40 mixing state bins are employed to represent accumulation-mode aerosols, including BC-free particles and various BC-containing particles[35,57,68]. The CAM–ATRAS model achieves satisfactory performance against a wide range of surface, aircraft, and satellite observations, particularly within the AeroCom III (Aerosol Comparisons between Observations and Models) framework[18,46,67,69]. AeroCom III is an open international initiative aimed at better understanding global aerosols and their impact. The dataset produced by the 17 models participating in AeroCom III, including the CAM–ATRAS, has been extensively adopted across multidisciplinary studies[18,19].

In the CAM–ATRAS, accumulation-mode particles with dry diameters (D_p) ranging from 40 nm to 1250 nm were classified into 5 size bins. Then eight BC mixing state bins were further defined on the basis of the mass ratio of BC to total dry aerosols, ranging from 0% to 100%, as shown in Supplementary Fig. 13. Via the use of these 40 two-dimensional mixing state bins, the CAM–ATRAS simulated various aerosol processes, including emission, new particle formation, condensation, coagulation, activation into cloud droplets, aqueous-phase chemistry, and deposition[68–70]. The model setup aligned with AeroCom III[18]: emission data were taken from monthly anthropogenic emissions based on the Community Emissions Data System[8] and Global Fire Emissions Database (GFED) version 4.1[71] (https://www.globalfiredata.org/), in which wildfire emissions were explicitly defined. The simulations were conducted with a horizontal resolution of 1.9° latitude × 2.5° longitude, 30 vertical layers (extending up to ~40 km), and monthly average outputs for the 2008–2015 period[18,68–70].

Via the use of this model, we evaluated changes in the BC AAOD at 550 nm wavelength with and without considering multi–core BC particles. The analysis involved the following steps. (1) D_p and D_c were calculated on the basis of aerosol number concentrations, mass, and density of each aerosol composition of the 40 bins. (2) In the base scenario, D_p and D_c were used to run the Core–Shell Mie model and obtained E_{abs_CS}. (3) D_p and D_c were transformed into $n_{core,cal}$, M_1, M_2, and $M_1{\times}M_2$, which were then input into RF2 along with D_p/D_c, D_c, D_p, E_{abs_CS}, $n_{core,cal}$, M_1, M_2, and $M_1{\times}M_2$ to obtain E_{abs_DEMA} for each mixing state bin. (4) E_{abs_CS} and E_{abs_DEMA} were substituted into Eq. (8) to calculate the BC AAOD offline, BC AAOD$_{CS}$, and BC AAOD$_{DEMA}$,

respectively. The detailed workflow is shown in Supplementary Fig. 13. Matsui, et al.[57] demonstrated that BC AAOD results from offline calculations closely aligned with those from online simulations using the Core–Shell Mie model.

$$\text{BC AAOD} = \sum_{z=1}^{30} \sum_{k=1}^{40} (\rho_z N_{z,k} C_{abs,c,z,k} E_{abs,z,k}) dh_z \qquad (8)$$

where z denotes the 30 levels for height and k denotes the mixing state bins for BC-containing particles; dh and ρ are the grid cell height and air density for each level, respectively; N is the aerosol number concentration for each mixing state bin; $C_{abs,c}$ and E_{abs} are the same as those in Eq. (6).

Sensitivity analysis

We highlight the enhanced light absorption ability resulting from multi–core BC particles while acknowledging the potential overestimation in the findings of E_{abs} simulations due to the nonsphericity of BC at low D_p/D_c values[10,20]. An experiment by Liu, et al.[10] revealed that the measured E_{abs} value approached 1 for $D_p/D_c < 1.4$, but the modelled E_{abs_CS} value increased with increasing D_p/D_c. We set E_{abs_CS} and E_{abs_DEMA} at 1 for $D_p/D_c < 1.4$ and then substituted E_{abs_CS} and E_{abs_DEMA} into Eq. 8 for $D_p/D_c > 1.4$ to calculate BC AAOD again; these values were referred to as BC AAOD$^*_{CS}$ and BC AAOD$^*_{DEMA}$, respectively. We estimated the contribution ratio using Eq. (9) to assess the relative importance of the global BC AAOD simulation due to nonsphericity and multi–core BC.

$$\text{Contribution ratio} = \frac{\text{BC AAOD}^*_{DEMA} - \text{BC AAOD}^*_{CS}}{\text{BC AAOD}_{CS} - \text{BC AAOD}^*_{CS}} \qquad (9)$$

Data availability

The Fire Information during the sampling period is provided by https://firms.modaps.eosdis.nasa.gov/map/. The observation and simulation data generated in this study have been deposited in the Figshare database [https://doi.org/10.6084/m9.figshare.28225802][72]. CAM-ATRAS model simulation results are available upon request from the author (H.M.). The transmission electron microscopy images are available from the corresponding authors upon request.

Code availability

Code for modelling absorption with DEMA–Mie is available from the author (M.J.). The Mie optical calculations are performed with PyMieScatt, which is available at https://github.com/bsumlin/PyMieScatt. 72-h backward trajectories are performed by MeteoInfo_3.5.2 (http://meteothink.org/). The code of the EMBS is available online (https://doi.org/10.6084/m9.figshare.13606304). The source code of DDA (DDSCAT 7.3.3) can be obtained online (http://ddscat.wikidot.com/). Code related to the RF1 and RF2 is available at [https://doi.org/10.6084/m9.figshare.28225802][72]. Additional code may be requested from the corresponding authors.

References

1. Jacobson, M. J. & Kaufman, Y. J. Wind reduction by aerosol particles. *Geophys. Res. Lett.* **33**, L24814 (2006).
2. Ding, A. J. et al. Enhanced haze pollution by black carbon in megacities in China. *Geophys. Res. Lett.* **43**, 2873–2879 (2016).
3. Coppola, A. I. et al. The black carbon cycle and its role in the Earth system. *Nat. Rev. Earth Environ.* **3**, 516–532 (2022).
4. Ding, K., et al. Aerosol-boundary-layer-monsoon interactions amplify semi-direct effect of biomass smoke on low cloud formation in Southeast Asia. *Nat. Commun.* **12**, 6416 (2021).
5. Xu, R. et al. Global population exposure to landscape fire air pollution from 2000 to 2019. *Nature* **621**, 521–529 (2023).
6. Bond, T. C. et al. Bounding the role of black carbon in the climate system: a scientific assessment. *J. Geophys. Res. Atmos.* **118**, 5380–5552 (2013).
7. Xu, H. et al. Updated global black carbon emissions from 1960 to 2017: improvements, trends, and drivers. *Environ. Sci. Technol.* **55**, 7869–7879 (2021).
8. Hoesly, R. M. et al. Historical (1750–2014) anthropogenic emissions of reactive gases and aerosols from the Community Emissions Data System (CEDS). *Geosci. Model Dev.* **11**, 369–408 (2018).
9. Jones, M. W. et al. Global rise in forest fire emissions linked to climate change in the extratropics. *Science* **386**, eadl5889 (2024).
10. Self, E. C. et al. Black-carbon absorption enhancement in the atmosphere determined by particle mixing state. *Nat. Geosci.* **10**, 184–188 (2017).
11. Cappa, C. D. et al. Radiative absorption enhancements due to the mixing state of atmospheric black carbon. *Science* **337**, 1078–1081 (2012).
12. Jacobson, M. Z. A physically-based treatment of elemental carbon optics: implications for global direct forcing of aerosols. *Geophys. Res. Lett.* **27**, 217–220 (2000).
13. Jacobson, M. Z. Strong radiative heating due to the mixing state of black carbon in atmospheric aerosols. *Nature* **409**, 695–697 (2001).
14. Sumlin, B. J., Heinson, W. R. & Chakrabarty, R. K. Retrieving the aerosol complex refractive index using PyMieScatt: a Mie computational package with visualization capabilities. *J. Quant. Spectrosc. Radiat. Transf.* **205**, 127–134 (2018).
15. Li, W. et al. Microphysical properties of atmospheric soot and organic particles: measurements, modeling, and impacts. *npj Clim. Atmos. Sci.* **7**, 65 (2024).
16. Lund, M. T. et al. Concentrations and radiative forcing of anthropogenic aerosols from 1750 to 2014 simulated with the OsloCTM3 and CEDS emission inventory. *Geosci. Model Dev.* **11**, 4909–4931 (2018).
17. Chiu, R. Y. et al. Exploiting simultaneous observational constraints on mass and absorption to estimate the global direct radiative forcing of black carbon and brown carbon. *Atmos. Chem. Phys.* **14**, 10989–11010 (2014).
18. Sand, M. et al. Aerosol absorption in global models from AeroCom phase III. *Atmos. Chem. Phys.* **21**, 15929–15947 (2021).
19. Chen, C. et al. Multi-angular polarimetric remote sensing to pinpoint global aerosol absorption and direct radiative forcing. *Nat. Commun.* **13**, 7459 (2022).
20. Fierce, L. et al. Radiative absorption enhancements by black carbon controlled by particle-to-particle heterogeneity in composition. *Proc. Natl Acad. Sci. USA* **117**, 5196–5203 (2020).
21. Chen, G., Liu, C., Wang, J., Yin, Y. & Wang, Y. Accounting for black carbon mixing state, nonsphericity, and heterogeneity effects in its optical property parameterization in a climate model. *J. Geophys. Res. Atmospheres* **129**, e2024JD041135 (2024).
22. Zeng, L. et al. Overestimation of black carbon light absorption due to mixing state heterogeneity. *npj Clim. Atmos. Sci.* **7**, 2 (2024).
23. Zhao, G., Tan, T., Zhu, Y., Hu, M. & Zhao, C. Method to quantify black carbon aerosol light absorption enhancement with a mixing state index. *Atmos. Chem. Phys.* **21**, 18055–18063 (2021).
24. Che, H. et al. Seasonal variations in fire conditions are important drivers in the trend of aerosol optical properties over the southeastern Atlantic. *Atmos. Chem. Phys.* **22**, 8767–8785 (2022).
25. Sedlacek, A. J. et al. Using the black carbon particle mixing state to characterize the lifecycle of biomass burning aerosols. *Environ. Sci. Technol.* **56**, 14315–14325 (2022).
26. Schwarz, J. P. et al. Measurement of the mixing state, mass, and optical size of individual black carbon particles in urban and biomass burning emissions. *Geophys. Res. Lett.* **35**, 33968 (2008).
27. Zhao, W. et al. Measurement report: size-resolved mass concentration of equivalent black carbon-containing particles larger

than 700 nm and their role in radiation. *Atmos. Chem. Phys.* **23**, 14889–14902 (2023).

28. Wang, J. et al. Significant contribution of coarse black carbon particles to light absorption in North China Plain. *Environ. Sci. Technol. Lett.* **9**, 134–139 (2022).

29. Yus-Díez, J. et al. Absorption enhancement of black carbon particles in a Mediterranean city and countryside: effect of particulate matter chemistry, ageing and trend analysis. *Atmos. Chem. Phys.* **22**, 8439–8456 (2022).

30. Mikhailov, E. F., Vlasenko, S. S., Podgorny, I. A., Ramanathan, V. & Corrigan, C. E. Optical properties of soot–water drop agglomerates: an experimental study. *J. Geophys. Res. Atmospheres* **111**, D07209 (2006).

31. Li, H. et al. Relationship between light absorption properties of black carbon and aerosol origin at a background coastal site. *Sci. Total Environ.* **886**, 163863 (2023).

32. Wang, Q. et al. Sources and physicochemical characteristics of black carbon aerosol from the Southeastern Tibetan Plateau: internal mixing enhances light absorption. *Atmos. Chem. Phys.* **18**, 4639–4656 (2018).

33. Fuller, K. A., Malm, W. C. & Kreidenweis, S. M. Effects of mixing on extinction by carbonaceous particles. *J. Geophys. Res. Atmospheres* **104**, 15941–15954 (1999).

34. Chýlek, P., Ramaswamy, V. & Cheng, R. J. Effect of graphitic carbon on the albedo of clouds. *J. Atmos. Sci.* **41**, 3076–3084 (1984).

35. Jacobson, M. Z. Investigating cloud absorption effects: global absorption properties of black carbon, tar balls, and soil dust in clouds and aerosols. *J. Geophys. Res. Atmospheres* **117**, D06205 (2012).

36. Jacobson, M. Z. Short-term effects of controlling fossil-fuel soot, biofuel soot and gases, and methane on climate, Arctic ice, and air pollution health. *J. Geophys. Res. Atmospheres* **115**, D14209 (2010).

37. Fan, M. et al. Nonlinear enhancement of radiative absorption by black carbon in response to particle mixing structure. *Geophys. Res. Lett.* **48**, 96437–97697 (2021).

38. Chen, X. et al. Quantifying evolution of soot mixing state from transboundary transport of biomass burning emissions. *iScience* **26**, 108125 (2023).

39. June, N. A. et al. Aerosol size distribution changes in FIREX-AQ biomass burning plumes: the impact of plume concentration on coagulation and OA condensation/evaporation. *Atmos. Chem. Phys.* **22**, 12803–12825 (2022).

40. Sakamoto, K. M. et al. Aged boreal biomass-burning aerosol size distributions from BORTAS 2011. *Atmos. Chem. Phys.* **15**, 1633–1646 (2015).

41. Hodshire, A. L. et al. Dilution impacts on smoke aging: evidence in Biomass Burning Observation Project (BBOP) data. *Atmos. Chem. Phys.* **21**, 6839–6855 (2021).

42. Sakamoto, K. M., Laing, J. R., Stevens, R. G., Jaffe, D. A. & Pierce, J. R. The evolution of biomass-burning aerosol size distributions due to coagulation: dependence on fire and meteorological details and parameterization. *Atmos. Chem. Phys.* **16**, 7709–7724 (2016).

43. Huang, K. et al. Superposition of Gobi dust and southeast asian biomass burning: the effect of multisource long-range transport on aerosol optical properties and regional meteorology modification. *J. Geophys. Res. Atmospheres* **124**, 9464–9483 (2019).

44. Liu, H. et al. Size-resolved mixing state and optical properties of black carbon at an urban site in Beijing. *Sci. Total Environ.* **749**, 141523 (2020).

45. Zhang, Y. et al. Strong haze-black carbon-climate connections observed across Northern and Eastern China. *J. Geophys. Res. Atmospheres* **128**, e2023JD038505 (2023).

46. Matsui, H. et al. Development and validation of a black carbon mixing state resolved three-dimensional model: aging processes and radiative impact. *J. Geophys. Res. Atmospheres* **118**, 2304–2326 (2013).

47. Riemer, N., West, M., Zaveri, R. A. & Easter, R. C. Simulating the evolution of soot mixing state with a particle-resolved aerosol model. *J. Geophys. Res.* **114**, D09202 (2009).

48. Xu, L. et al. Tracing the evolution of morphology and mixing state of soot particles along with the movement of an Asian dust storm. *Atmos. Chem. Phys.* **20**, 14321–14332 (2020).

49. Flatau, P. J. & Draine, B. T. Fast near field calculations in the discrete dipole approximation for regular rectilinear grids. *Opt. Express* **20**, 1247–1252 (2012).

50. Corral Arroyo, P. et al. Amplification of light within aerosol particles accelerates in-particle photochemistry. *Science* **376**, 293–296 (2022).

51. Beeler, P. et al. Light absorption enhancement of black carbon in a pyrocumulonimbus cloud. *Nat. Commun.* **15**, 6243 (2024).

52. Jacobson, M. Z. Effects of externally-through-internally-mixed soot inclusions within clouds and precipitation on global climate. *J. Phys. Chem. A* **110**, 6860–6873 (2006).

53. Li, K. et al. Significantly accelerated photochemical and photocatalytic reactions in microdroplets. *Cell Rep. Phys. Sci.* **3**, 100917 (2022).

54. Kahnert, M., Nousiainen, T. & Lindqvist, H. Models for integrated and differential scattering optical properties of encapsulated light absorbing carbon aggregates. *Opt. Express* **21**, 7974–7993 (2013).

55. Beeler, P. & Chakrabarty, R. K. Constraining the particle-scale diversity of black carbon light absorptionusing a unified framework. *Atmos. Chem. Phys.* **22**, 14825–14836 (2022).

56. Riemer, N. & Bond, T. C. Toward reduced representation of mixing state for simulating aerosol effects on climate. *Bull. Am. Meteorol. Soc.* **98**, 971–980 (2017).

57. Matsui, H., Hamilton, D. S. & Mahowald, N. M. Black carbon radiative effects highly sensitive to emitted particle size when resolving mixing-state diversity. *Nat. Commun.* **9**, 3446 (2018).

58. Wang, Z., Zhang, H., Li, J., Jing, X. & Lu, P. Radiative forcing and climate response due to the presence of black carbon in cloud droplets. *J. Geophys. Res. Atmospheres* **118**, 3662–3675 (2013).

59. Lauritsen, S. M. et al. Explainable artificial intelligence model to predict acute critical illness from electronic health records. *Nat. Commun.* **11**, 3852 (2020).

60. Ching, J., Fast, J., West, M. & Riemer, N. Metrics to quantify the importance of mixing state for CCN activity. *Atmos. Chem. Phys.* **17**, 7445–7458 (2017).

61. Wang, Y. et al. Fractal dimensions and mixing structures of soot particles during atmospheric processing. *Environ. Sci. Technol. Lett.* **4**, 487–493 (2017).

62. Abo Riziq, A., Erlick, C., Dinar, E. & Rudich, Y. Optical properties of absorbing and non-absorbing aerosols retrieved by cavity ring down (CRD) spectroscopy. *Atmos. Chem. Phys.* **7**, 1523–1536 (2007).

63. Sihvola, A. & Sharma, R. Scattering corrections for Maxwell Garnett mixing rule. *Microw. Opt. Technol. Lett.* **22**, 229–231 (1999).

64. Bond, T. C. & Bergstrom, R. W. Light absorption by carbonaceous particles: an investigative review. *Aerosol Sci. Technol.* **40**, 27–67 (2007).

65. Sorensen, C. M. & Fischbach, D. J. Patterns in Mie scattering. *Opt. Commun.* **173**, 145–153 (2000).

66. Aas, K., Jullum, M. & Løland, A. Explaining individual predictions when features are dependent: more accurate approximations to Shapley values. *Artif. Intell.* **298**, 103502 (2021).

67. Gliß, J. et al. AeroCom phase III multi-model evaluation of the aerosol life cycle and optical properties using ground- and space-based remote sensing as well as surface in situ observations. *Atmos. Chem. Phys.* **21**, 87–128 (2021).

68. Matsui, H. & Mahowald, N. Development of a global aerosol model using a two-dimensional sectional method: 2. Evaluation and sensitivity simulations. *J. Adv. Model. Earth Syst.* **9**, 1887–1920 (2017).

69. Matsui, H. et al. Contrasting source contributions of Arctic black carbon to atmospheric concentrations, deposition flux, and atmospheric and snow radiative effects. *Atmos. Chem. Phys.* **22**, 8989–9009 (2022).

70. Matsui, H. Development of a global aerosol model using a two-dimensional sectional method: 1. model design. *J. Adv. Model. Earth Syst.* **9**, 1921–1947 (2017).

71. van der Werf, G. R. et al. Global fire emissions estimates during 1997–2016. *Earth Syst. Sci. Data* **9**, 697–720 (2017).

72. Chen, X. *Locating the missing absorption enhancement due to multi-core black carbon aerosols*, Figshare, https://doi.org/10.6084/m9.figshare.28225802, 2025.

Acknowledgements

Author contributions

X.C. and W.L. conceived the overall idea and performed most of the analysis and model simulations; Z.Z., F.Z., Y.W., X.C., and W.L. drafted the paper; D.L., S.Z., Y.R., Z.S., H.Y., and K.J. edited the paper; X.C. and F.W. collected the samples; X.C., H.Y., and K.J. conducted single particle analysis; J.C., H.M., and M.J. conducted the simulations.

Competing interests

The authors declare no competing interests.

Additional information